

Geological mapping in semi-arid regions with low spectral contrast surfaces using ASTER data

Mourad El Koundi^{1,2}, Pascal Allemand³, Fouad Zargouni²

¹(Office National des Mines, 24 Rue de l'Energie, La Charguia 2035, Tunis, Tunisia)

²(Département de Géologie, Faculté des Sciences de Tunis, 1060 El Manar II, Tunis, Tunisia)

³(Université de Lyon, F-69622, Lyon, France, Université Lyon 1, Villeurbanne, ENS, Lyon)

Abstract: Advanced Spaceborne Thermal Emission Reflection Radiometer (ASTER) is largely used for geological mapping and lithological discriminations because of its relative fine resolution and its relative broad spectral range (14 bands). This study investigated the use of ASTER data for geological mapping at scale 1:50.000 in the Sahel block (eastern Tunisia). This region is characterised by sedimentary outcropping series with relative low tone contrast. Based on mineral composition of outcropping series, five indices were used in addition to VNIR and SWIR corrected bands for classification process. A Minimum Noise Fraction Transformation was performed to increase S/N ratio and to reduce redundancy. Eleven spectral endmembers representing lithostratigraphic units were used as training classes for a supervised classification using the Spectral Angle Mapping (SAM) algorithm. Results were validated using field verification and accuracy assessment. With an overall accuracy of 85.67% and a Kappa of 0.791, produced map is estimated to be accurate.

Keywords – ASTER, geological mapping, spectral analysis, spectral low contrast surfaces, Tunisian Sahel

I. Introduction

ASTER is a high spatial resolution-imaging instrument on board the NASA's Earth Observing System Terra satellite. It acquires imagery from 14 different spectral bands by mean of three separate subsystems. The first one measures reflected radiation in three bands ranging from 0.52 to 0.86 μm (VNIR) with spatial resolution of 15m. The second subsystem (SWIR) has six spectral channels ranging from 1.6 to 2.43 μm (SWIR) with spatial resolution of 30m. The third one (TIR) measures emitted radiation in five bands in the 8.125 – 11.65 μm wavelength regions at 90m resolution. In addition, ASTER has fine stereoscopic capabilities useful for geological and geomorphological studies thanks to a back-looking VNIR telescope with 15m resolution [1]. The swath-width is 60 km and its pointing capability extends the total cross-track viewing capability to 232 km [2, 3]. This complimentary combination of both spectral and geometrical properties provides to ASTER high mineral discrimination capabilities.

ASTER has already proved its ability for mapping lithologies on spectral contrasted surfaces. In fact, VNIR data were used for chlorophyll density estimation and for Iron and some rare-earth element detection [4, 5]. SWIR data offer the possibility for carbonate, hydrate and hydroxide mineral mapping [4, 6]. Thanks to its sensitivity to emissions in thermal infrared region, ASTER can also spectrally separate quartzose rocks, granitic rocks and intermediate to mafic rocks [4].

Many studies evaluating potential of ASTER data in discriminating minerals and mapping rock types were largely described [7-10]. These studies often use in-place spectral data, hyperspectral data or both combinations and it generally concerns areas with high contrast spectra.

This paper tests the capabilities of ASTER data to validate and extent existing geological maps at 1:50000 scale in the Sahel block (Eastern Tunisia). Only spectral libraries of known "pure" materials are used to correlate outcropping series spectra with mixture materials. These compositions encloses Calcite, Illite, Kaolinite, Gypsum and Quartz that are the most frequent minerals forming outcropping rocks in this region.

II. Geological and geomorphological settings

The Tunisian Sahel (Eastern Tunisia) is a semi-arid area of low steppes characterized by flat slowly subsiding lowlands and formed by low hills, flat plains and large sebkhas separated by a dense hydrographic network [11-13]. The National Geological Survey of Tunisia attaches an interest in mapping this region because of its relative low coverage rate at 1/50.000 scale.

The Sahel outcropping series comprises only sedimentary units made by monotonous series with alternating sand, clay and limestone. Distinction between some units is difficult because of alteration that causes the formation of calcareous crust and carbonate concretions on sandy or clayey area [13]. Over 80% of the Sahel surface is represented by continental quaternary deposits that should be differentiated to produce more detailed and precise geological maps.

The study area (Fig. 1) is located in the southern part of the Tunisian Sahel longitudes (09° 55' 27.3" E to the West and 10° 53' 13.0" E to the East) and latitudes (35° 04' 34.6" N to the North and 34° 30' 35.0" N to the south) for an area of 20 by 20km². This sector covers the common corners of four geological maps at 1/50.000 scale of Bir Ali Ben Khalifa (No. 105) of Agareb (No. 106) Graiba (No. 114) and Mahares (No. 115).

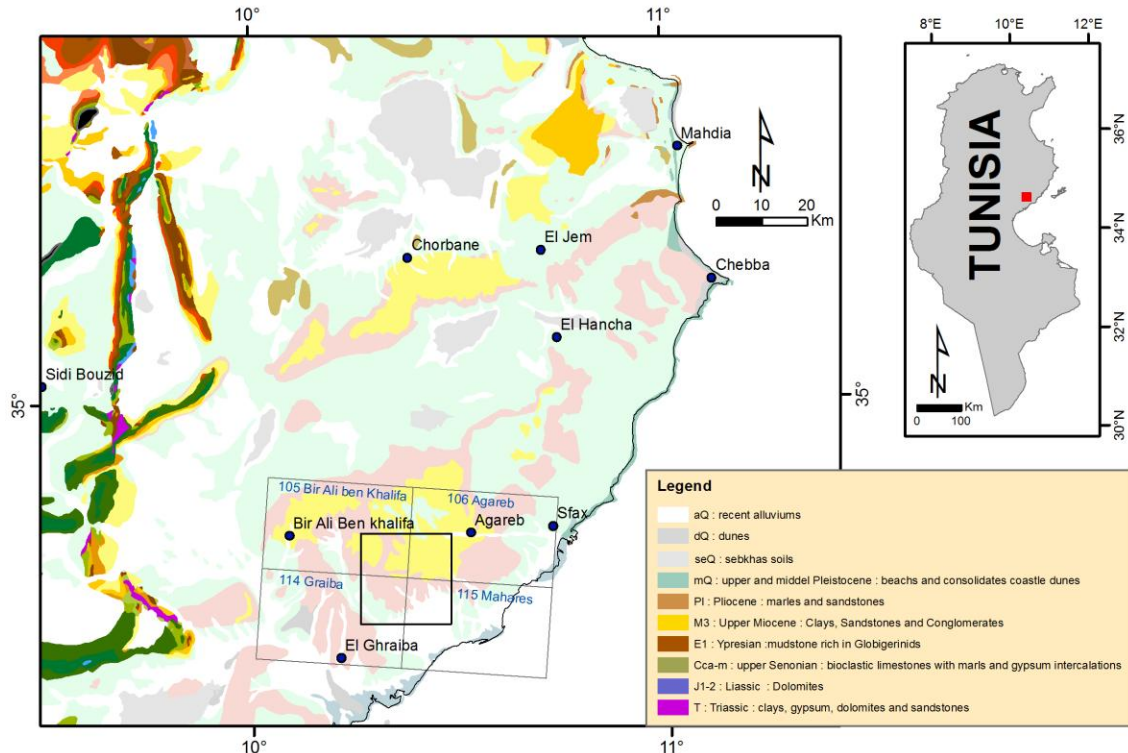


Fig. 1: Geological map of Tunisian Sahel [14]

The sedimentary outcropping series predominantly consist of Quaternary deposits with Upper Miocene to Pliocene rare outcrops [13, 15]. Mio-Pliocene deposits (M-Pl) are undifferentiated on geological maps at 1/50.000 scale. It consist of alternating yellow fine grained sand and brownish clay [16-18]. Pliocene series (Plm) are formed by yellowish gypsiferous clay that overlay M-Pl in continuity of sedimentation (ie. no evident sedimentary or tectonic limit). The Quaternary deposits are widespread and represented by various continental deposits (Fig. 2). Associated lithological units are subdivided to three groups: 1) Lower Pleistocene (Qv) with silt and red shale slightly gypseous and capped by a calcareous crust known as “villafranchian crust”. 2) The middle Pleistocene deposits that occupy the majority of the high zones and show reddish silts and soils with limestone concretions (Qcl) and a lot of blocks of the “villafranchian” crust (Qe) [16, 19]. 3) The upper Pleistocene deposits are more developed than the two previous series; they are formed dominantly by reddish sands (IQ) with diffuse carbonated and gypsiferous concretions and sand with altered elements, such as conglomeratic beds (Qg) [17]. Historic to Actual deposits are formed by aeolian sand (dQ) and Wadi-fills (a) with sand, clay and gravel (Fig.2).

Two geological maps were established in the eastern part of study area [16, 17]. To report lithostratigraphic limits of these units, cartographers are only guided by topographic contour lines and geomorphological features so that produced maps become contestable. Although having varied percentages in mineral composition, these units present nearly the same shaly and sandy facies. For cartographers lithostratigraphic units are hard to discriminate and precisely map with only field observation or photo-interpretation.

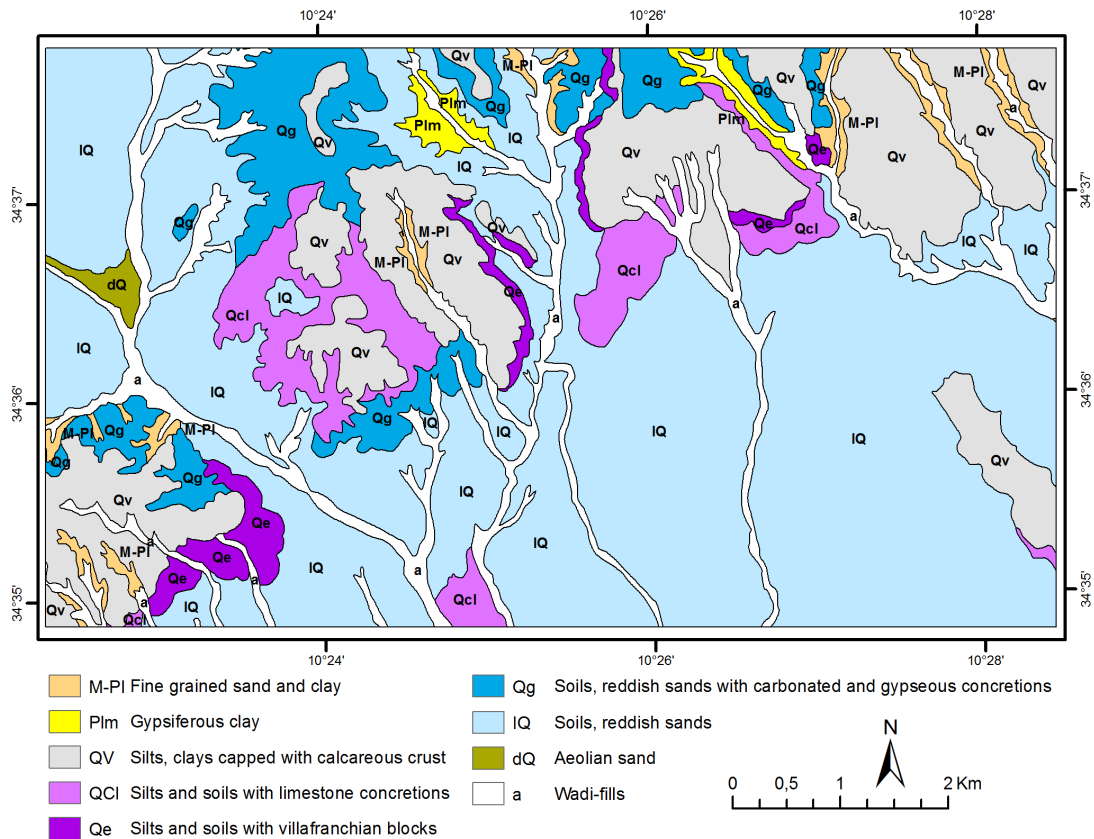


Fig. 2: Geological map of Mahares [17]

III. Methods

For several decades, many studies used multispectral imaging data in general and ASTER data specially to map lithology or mineral distribution using several methodologies [20-22]. These studies concern, generally, high spectral contrasted areas with “sub-pure” pixels and use hyperspectral data or field measured spectra to identify endmembers and to improve classification process. Spectral libraries of known materials make it possible to correlate study area series with different mineral mixtures.

Two types of approaches are frequent on related literature. The first one uses the spectral signatures of minerals or mixtures (rocks, vegetation ...) to identify and map their spatial distribution. This process involves: 1) Minimum Noise Fraction (MNF) transformation to enhance data quality by increasing signal to noise ratio, 2) Pixel Purity Index (PPI) algorithm to locate most pure pixels, 3) endmembers identification, and 4) map production using a classification process.

The second type of methods make use of the distinguishing spectral characteristics of some rocks or mixtures to increase the spectral contrast value. Basing on the lithological composition of outcropping series, other authors suggest using band ratios [4, 10, 23, 24].

Within this work, and going with mineral composition of outcrops that are made by calcite, illite, kaolinite, smectite, gypsum and quartz [16, 19], five band ratios were used.

The Carbonate Index (CI) was defined by [25] to map extension of calcareous and dolomitic rocks that show an absorption feature at 11.3 μm region that corresponds to ASTER band 14. The carbonate index is computed using the following formula:

$$CI = B13/B14$$

The Quartz Index (QI) was also defined by [25] to map the silica minerals that show a relatively higher emissivity at 8.65 μm (ie ASTER band 11) than at 8.3 μm (ie ASTER band 10) and at 9.1 μm (ie ASTER band 12) (Fig. 4). QI is calculated as follows:

$$QI = B11 \times B11 / B10 \times B12$$

QI is expected to be high for quartz and low for K-feldspar and gypsum.

Many clayey minerals (illite and kaolinite) display a strong feature in SWIR region at 2.2 μm (ie ASTER band 6) assigned to a combination mode of OH in clay lattice [26]. The Clay Index (CII) is proposed by [27] and was computed using the following formula:

$$CLI = B5 \times B7 / B6 \times B6$$

The Normalized Difference Vegetation Index (NDVI), was proposed by [28] following this formula :

$$NDVI = (NIR - R) / (NIR + R)$$

Where “NIR” is data collected from the near-infrared part of the spectrum (ie ASTER band 3) and “R” that from the red part of the spectrum (ie ASTER band 2). Any kind of ASTER data can be applied to extract NDVI [29]. For this study, the Level-1B data are used this index was also used to select the appropriate Regions Of Interest (ROIs) at the endmember selection step.

The Roughness Index (RI) is introduced by [24] as the topographic expression of the surface below maps resolution and following this formula:

$$RI = B3B/B3N$$

The roughness index is used to increase spectral contrast between lithostratigraphic pair units that possess nearly the same lithologic composition and differ only by presence of gravel or rock blocs (Qcl – Qe).

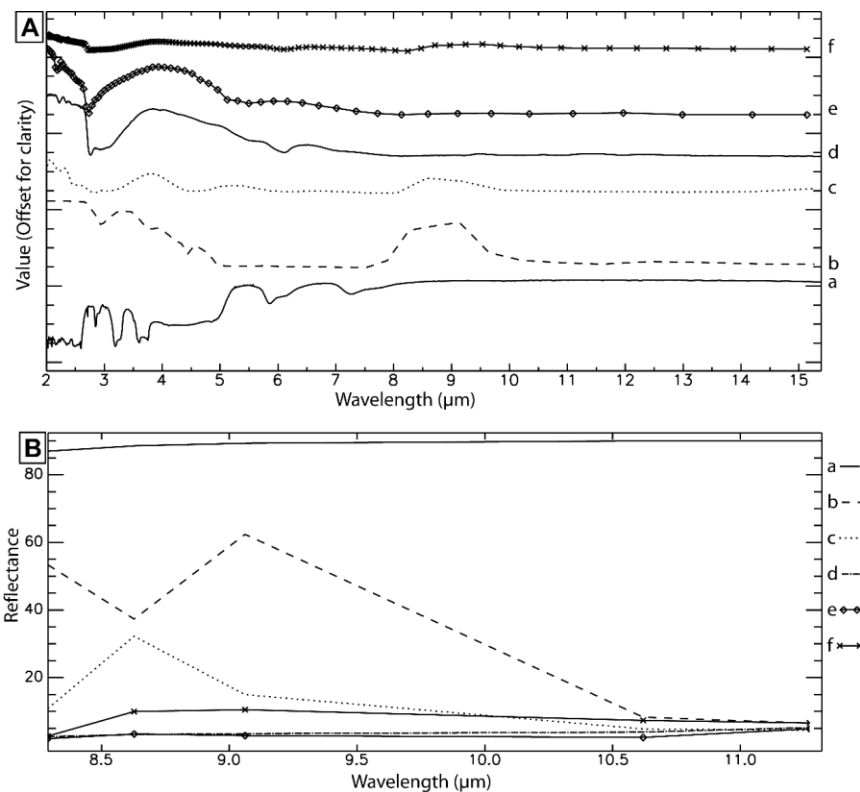


Fig. 3: Laboratory based emissivity spectra of: a) calcite, b) quartz, c) gypsum, d) illite, e) kaolinite and f) smectite which are dominant in the study area; A- Full resolution spectrum; B- resampled spectrum to ASTER TIR wavelengths. Notice that all pairs except the illite-kaolinite one can easily be distinguished with ASTER data

The applied approach consists of using both of the previously defined methods. We propose to integrate significant band ratios previously listed in order to maximize contrast values at the classification step. The analysis approach (Fig. 4) comprises a pre-processing step that concerns all ASTER bands (B1-B14) except the back-looking band 3 (B3B) and a processing step that concerns all pre-processed output data with the B3B band. It includes all band ratios computation, the Minimum Noise Fraction (MNF) transform, the endmember selection and the classification procedure.

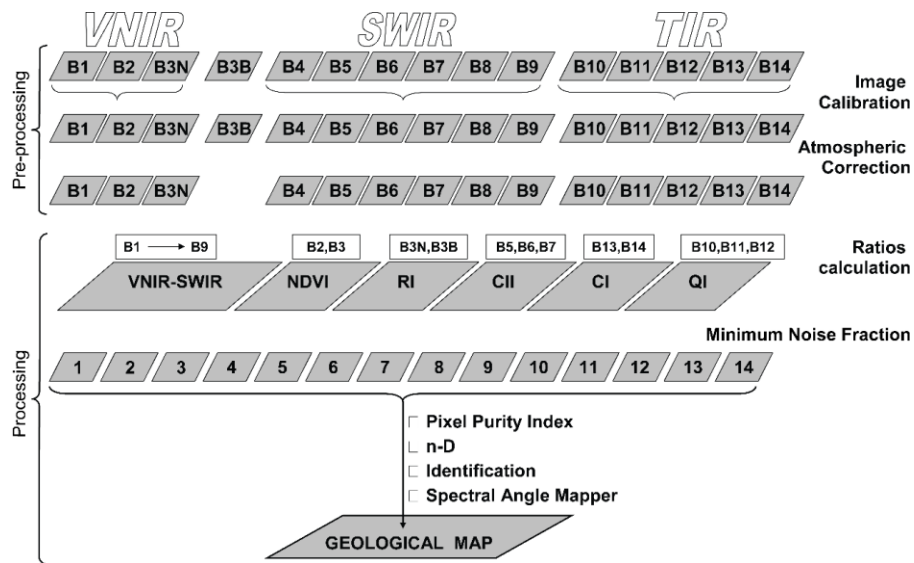


Fig. 4: Classification approach steps. The Hourglass approach processing steps were not only applied on calibrated VNIR and SWIR ASTER data (B1-B9), five band ratios (NDVI, RI, CII, CI, and QI) were also computed and injected as input data to the classification procedure

3.1 Aster Data Pre-Processing

The used ASTER scene (AST_L1B_00305052003101258_20061018110915_16045) is cloud free level 1B data that acquired on May 05, 2003 with a solar incidence angle of about 138.69° and an azimuth angle of about 66.9°. The image has been pre-georeferenced to Universal Transverse Mercator (Zone 32 North) with WGS-84 datum.

The following pre-processing steps were performed: 1) Crosstalk correction; 2) Stacking and co-registration of all 14 bands; 3) Atmospheric correction using the FLAASH module within the Environment for Visualizing Images (ENVI) software [30, 31]; 4) Topographic correction and (5) Image orthorectification using SRTM 1 Arc-Second DEM data.

3.2 Aster Data processing

Several consecutive processes were performed to produce a calibrated reflectance/emission images that go with known spectral libraries. Data analysis are based on the fact that all bandwidths are considered as too narrow, making it possible to extract a spectrum from each pixel of image. This spectrum is compared to other “pure” materials spectra (minerals, rocks, vegetation ...) endmembers. To extract accurately endmembers, a Minimum Noise Fraction (MNF) transform is applied to enhance data quality by increasing S/N ratio and reducing data redundancy and correlation between spectral bands [32-34].

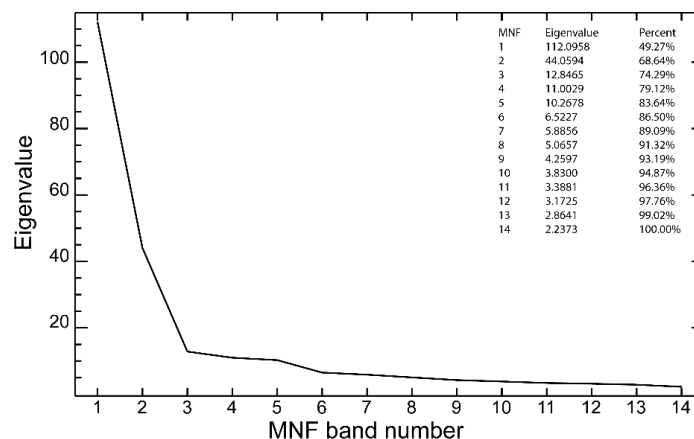


Fig. 5: MNF eigenvalues plot of the 14 eigenimages of the ASTER data

Furthermore, to evaluate the separation quality of mapped lithostratigraphic units with MNF eigenimages, ROIs separability was calculated with Jeffries-Matusita (J-M) and Transformed Divergence separability coefficients (T.D.) [31]. Almost all values are lower than 1.6 (Table 1 **Error! Reference source not found.**) indicating average class-separability [35].

Table 1: ROIs separability coefficients

| | | M-Pl | Plm | QV | Qd | Qe | Qg | IQ | a |
|-------------|------|-------------|-------------------|-------------------|-------------------|-------------------|-------------------|-------------------|-------------------|
| M-Pl | J-M | | <u>0.74887089</u> | <u>0.30935456</u> | <u>0.95838688</u> | <u>0.43178234</u> | <u>0.52713492</u> | 1.37285648 | <u>0.82731323</u> |
| | T.D. | | <u>0.84172188</u> | <u>0.32008294</u> | 1.05663537 | <u>0.45131492</u> | <u>0.57229856</u> | 1.49185064 | <u>0.91318144</u> |
| Plm | J-M | | | <u>0.84369972</u> | 1.05458838 | 1.00363865 | <u>0.33826179</u> | 1.72616238 | 1.26829366 |
| | T.D. | | | <u>0.95072599</u> | 1.23236322 | 1.17869774 | <u>0.35636109</u> | 1.87715048 | 1.51036746 |
| QV | J-M | | | | <u>0.90971484</u> | <u>0.34908795</u> | <u>0.64379738</u> | 1.39244959 | <u>0.85123897</u> |
| | T.D. | | | | 1.05615005 | <u>0.36281634</u> | <u>0.78344159</u> | 1.53034701 | <u>0.95935011</u> |
| Qd | J-M | | | | | <u>0.76189490</u> | <u>0.81249619</u> | 1.02625640 | <u>0.49924943</u> |
| | T.D. | | | | | <u>0.93706019</u> | <u>0.90358980</u> | 1.15234905 | <u>0.53947726</u> |
| Qe | J-M | | | | | | <u>0.83873862</u> | 1.08187765 | <u>0.57438006</u> |
| | T.D. | | | | | | 1.00480166 | 1.19475459 | <u>0.64715590</u> |
| Qg | J-M | | | | | | | 1.56051515 | 1.06807006 |
| | T.D. | | | | | | | 1.68757486 | 1.22973233 |
| IQ | J-M | | | | | | | | <u>0.46787249</u> |
| | T.D. | | | | | | | | <u>0.50701417</u> |
| a | J-M | | | | | | | | |
| | T.D. | | | | | | | | |

Notice that many pair values (underlined) are lower than one and indicate a poor separability between ROI pairs and high mixture level. Only Plm and IQ (bolded pair) are relatively well distinguishable from one to other with a T.D. value over 1.8 and a J-M value over 1.7.

Manually extracting pure pixels is a hard and time-consuming task because most imagery pixels are not pure and often bear a relative influence of adjacent materials.

PPI is an automatic mean of identification of most pure pixels that is used for lithological mapping because it produces a lithologic high separation within ASTER images [4, 36]. After, applying PPI thresholding, a visual selection of “pure pixels” allowed defining image classes [34, 37, 38]. For the study area, 11 endmembers were used in the classification procedure (Table 2). Some class-types are equivalent to geological map units (M-Pl, Plm, Qv, Qcl, Qe and Qg), others (IQ and a) were each subdivided into two subclasses because of their important lithologic variation. In fact, IQ may be in places, covered with thick aeolian sand (dQ) that must be limited.

Table 2: ASTER mapping classes

| N° | Map unit | Image class | Pixel number | Lithological composition |
|----|----------|-------------|--------------|--|
| 1 | M-Pl | M-Pl | 58 | Fine grained sand and brownish clay |
| 2 | Plm | Plm | 71 | yellowish gypsiferous clay |
| 3 | QV | QV | 118 | Silts and clays capped with calcareous crust |
| 4 | Qcl | Qcl | 120 | Silts and soils with limestone concretions |
| 5 | Qe | Qe | 105 | Silts and soils with villafranchian blocks |
| 6 | Qg | gQ | 147 | Soils and reddish sands with carbonated and gypseous concretions |
| 7 | IQ | IQ1 = (IQ) | 131 | Soils and reddish sands |
| 8 | | IQ2 = (dQ) | 104 | Aeolian Sand |
| 9 | a | a | 138 | Sand and clay |
| 10 | | a2 | 109 | Gravel and heterogeneous blocs |
| 11 | | vegetation | 102 | Grass |

To validate endmembers selection, relating (J-M) and (T.D.) coefficients are computed for all MNF eigenimages pairs. All calculated values are greater than 1.9 indicating good class-separability [35].

The first step following the endmember collection and the validation of ROIs separability is to evaluate the classification ability of the procedure. For each endmember a spectral profile with statistics concerning minimum, maximum, mean and standard deviation of each MNF eigenimages are calculated. Resulting statistics prove that majority of the classes' pairs may be easily distinguished and differentiated by MNF eigenimages (Fig. 6). For example, the lithostratigraphic unit (a) can be easily differentiated from (a2) by large number of MNF eigenimages (1, 2, 3, 5, 8, and 9) and (lQ) can be clearly distinguished from (dQ) using four MNF eigenimages (1, 2, 6 and 8) however separation between (Qc1) and (Qe) is ambiguous (Fig. 6).

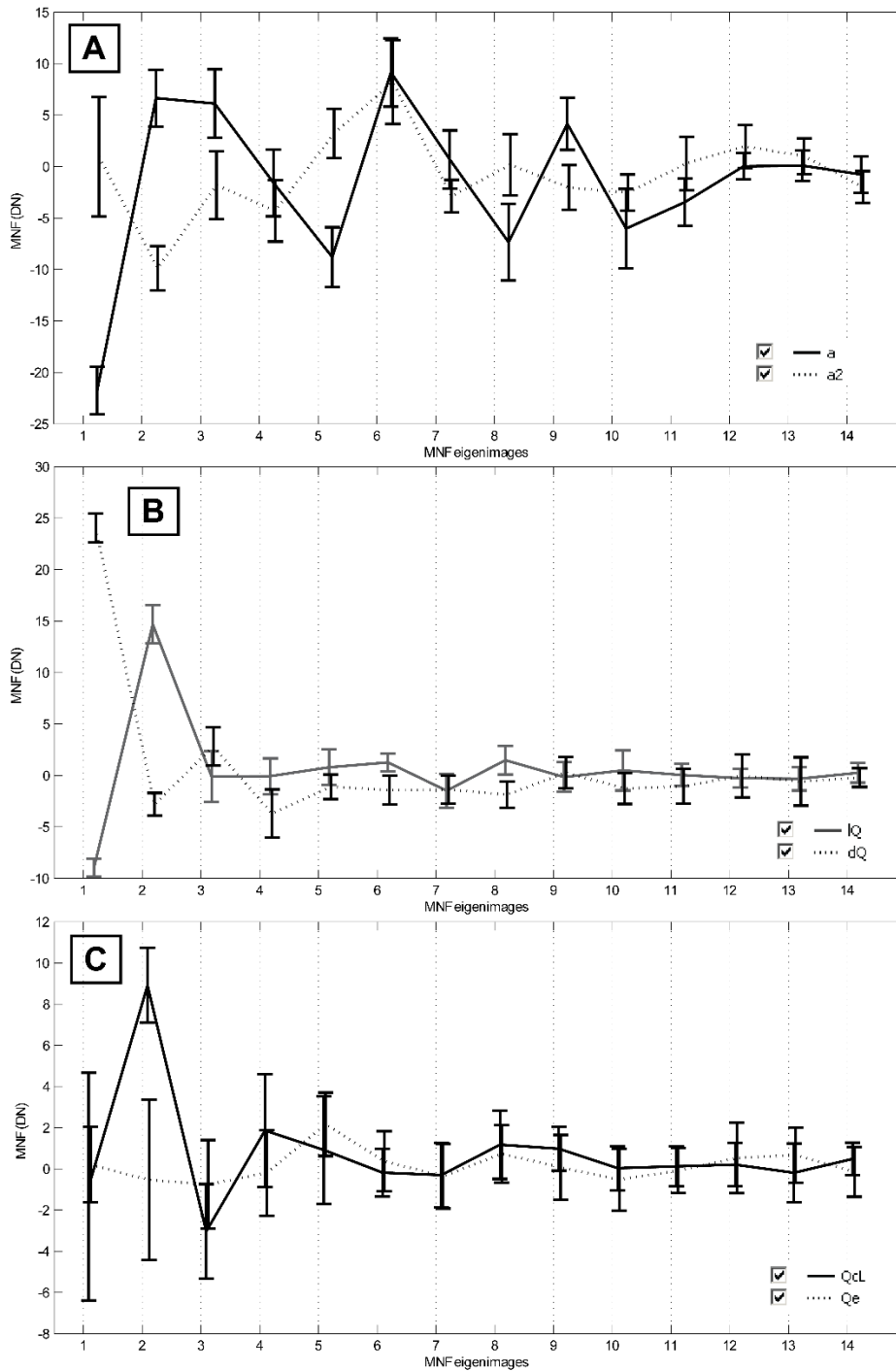


Fig. 6: a-a2 pair endmember spectral profile, B- lQ-dQ pair endmember spectral profile, C- QcL-Qe pair endmember spectral profile

Table 3: Endmembers pairs separation with MNF eigenimages

| | Plm | QV | Qd | Qe | Qg | IQ | dQ | a | a2 | Grass |
|------|------|---------|------------|------------|-------------------------|------------------|----------------------|-----------------------------|-------------------|-----------------------------|
| M-Pl | 8, 9 | 2, 8, 9 | 2, 7, 8, 9 | 1, 7, 8, 9 | 1, 2, 3, 6, 7, 8, 9, 10 | 2, 7, 8, 9 | 1, 4, 6, 7, 9 | 1, 2, 3, 5, 6, 8, 9, 10, 11 | 1, 2, 4, 6, 7, 10 | 1, 3, 5, 7, 9, 11 |
| Plm | | 2 | 2 | 1, 7 | 1, 2, 6, 7, 8, 9, 14 | 2, 7 | 1, 5, 6, 7, 8 | 1, 2, 3, 5, 6, 8, 9, 11 | 1, 6, 7 | 1, 3, 5, 7, 8, 9, 10, 11 |
| QV | | | 2, 7 | 1, 2, 7 | 1, 2, 3, 6, 7, 8, 9, 10 | 2, 7 | 1, 2, 4, 7, 8 | 1, 2, 5, 6, 8, 10, 11 | 4, 6, 7, 10, 14 | 1, 2, 3, 5, 6, 7, 8, 9, 11 |
| Qd | | | | 2 | 2, 6, 7, 8, 9, 10 | 1, 2 | 1, 2, 3, 4, 8 | 1, 3, 5, 6, 8, 10, 11 | 2, 4, 6, 14 | 1, 2, 3, 5, 6, 7, 8, 9, 11 |
| Qe | | | | | 2, 3, 6, 7, 8, 9 | 1, 2 | 1, 5, 8 | 1, 2, 3, 5, 6, 8, 9, 10, 11 | 2, 6 | 1, 3, 5, 6, 7, 8, 9, 11 |
| Qg | | | | | | 1, 2, 3, 6, 8, 9 | 1, 2, 3, 6, 8, 9, 14 | 1, 2, 3, 5, 11 | 2, 8, 9, 14 | 1, 2, 3, 5, 6, 7, 10, 11 |
| IQ | | | | | | | 1, 2, 6, 8 | 1, 2, 3, 5, 6, 8, 9, 10, 11 | 1, 2, 6 | 1, 2, 3, 5, 6, 7, 8, 9, 11 |
| dQ | | | | | | | | 1, 2, 5, 6, 8, 9 | 1, 2, 5, 6 | 1, 3, 5, 6, 7, 8, 9, 10, 11 |
| a | | | | | | | | | 1, 2, 3, 5, 8, 9 | 1, 3, 5, 7, 10, 11 |
| a2 | | | | | | | | | | 1, 2, 3, 5, 7, 8, 9, 10, 11 |

Table 3 indicates that B1 and B2 highly participate to the discriminatory abilities of ASTER data (B1:69.6% and B2:75%) whereas B12 and B13 were not used (Fig. 7).

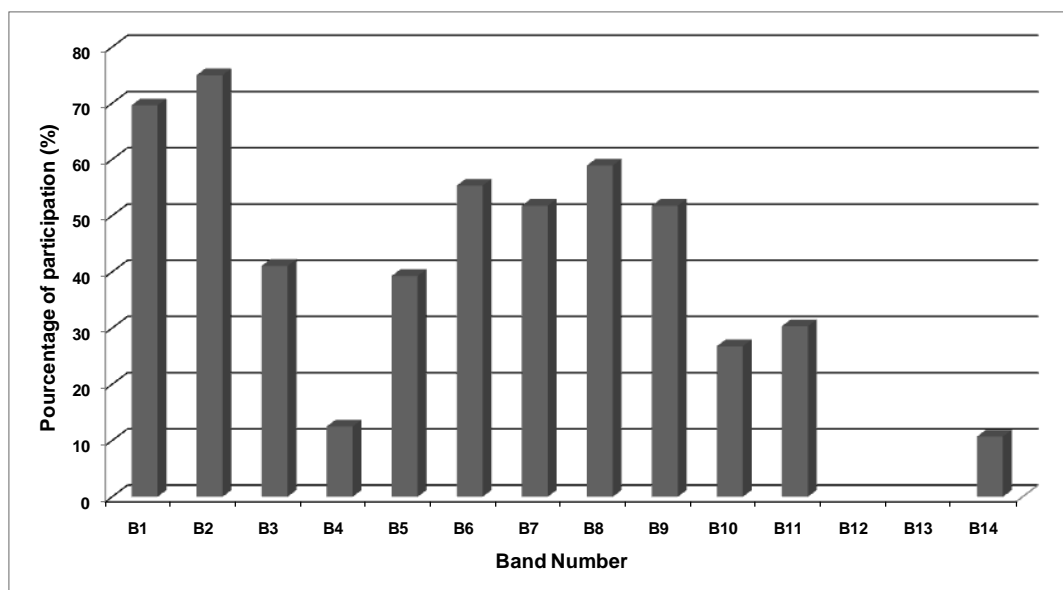


Fig. 7: Discriminatory abilities of MNF eigenimages. The y axis represent the percentage of participation of one band B(i) to distinguish all existing pairs (100% means that band (i) can distinguish all pairs)

3.3 Image classification

Spectral Angle Mapper (SAM) algorithm is used to generate the new geological map at 1/50.000 scale (Fig. 8) based on eleven endmembers that were used as training classes. For the quality control, the result is compared to the existing geological map. An average similarity is visually clear between limits of the classification result and those of the geological maps for the (Qv) and (IQ) units. All other units are classified with a weak correlation to geological maps. The percentage of unclassified pixels is 17.7%.

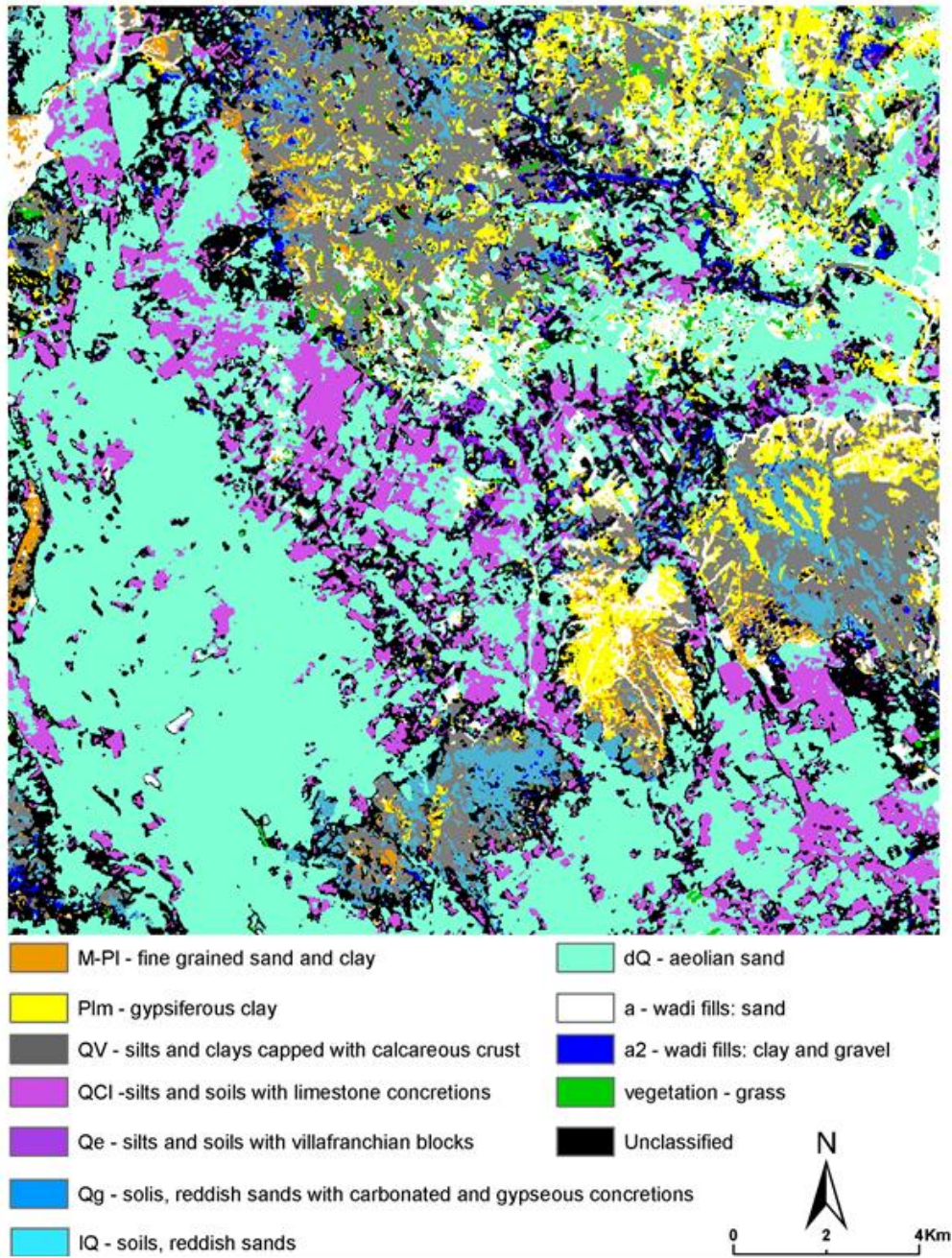


Fig. 8: Output classification map (3 x 3 majority filter to reduce noise)

IV. Results and discussion

Error or confusion matrix [39] is used to quantify accuracy by comparing results with ground truth information [40, 41]. As first step, existing geological maps were used as source of truth information. Subclasses (Qcl-dQ and a-a2) were merged to be in accordance with existing geological map units. The accuracy assessment table (Table 4) shows a low percentage of pixels accurately classified. The overall accuracy is 36.9629% and the Kappa Coefficient is 0.1866.

Table 4: accuracy assessment table

| Classification | M-PI (%) | Plm (%) | QV (%) | Qd (%) | Qe (%) | Qg (%) | IQ (%) | a (%) | User's accuracy |
|----------------|----------|---------|--------|--------|--------|--------|--------|-------|-----------------|
| M-PI | 1.68 | 2.25 | 7.08 | 5.7 | 3.54 | 5.03 | 0.44 | 1.57 | 1.68 |
| Plm | 12.51 | 30.45 | 9.2 | 10.93 | 15.19 | 23.21 | 1.57 | 2.22 | 30.45 |
| QV | 32.16 | 22.94 | 38 | 9.39 | 16.61 | 26.1 | 2.78 | 10.47 | 38.00 |
| Qd | 1.51 | 0.32 | 1.8 | 14.61 | 5.89 | 1.12 | 19.98 | 9.86 | 14.61 |
| Qe | 0.66 | 0.27 | 0.46 | 1.58 | 0.65 | 0.39 | 0.89 | 0.9 | 1.39 |
| Qg | 27.26 | 17.49 | 16.83 | 4.87 | 7.78 | 15.48 | 1.42 | 6.7 | 15.48 |

| | | | | | | | | | |
|----------------------------|------|------|-------|-------|-------|-------|-------|-------|-------|
| IQ | 3.76 | 1.89 | 4.41 | 25.22 | 15.11 | 4.97 | 50.67 | 37.95 | 50.67 |
| a | 6.61 | 18.3 | 9.75 | 9.58 | 6.75 | 14.08 | 3.01 | 8.28 | 8.28 |
| Producer's accuracy | 1.93 | 5.02 | 48.71 | 6.17 | 0.00 | 19.39 | 80.61 | 12.58 | |

Compared with existing geological maps at 1/50,000, final output classification map shows important differences. Many behaviours of lithology classification have been distinguished. The (M-Pl) and (Qe) units illustrate the case of very badly classified units with both User's and Producer's accuracy lower than 2%. The (Qcl), (Qg) and (a) lithostratigraphic units are roughly classified with both User's and Producer's accuracy lower than 20%. The (QV) unit is considered as moderately classified with both User's and Producer's accuracy lower than 70%. The Producer's accuracy of (IQ) unit is 80%, indicating many locations on geological maps were accurately identified with classification procedure, but some actual deposits (a) were also assigned to this unit class. In contrast, the User's accuracy of (Plm) unit was 30% but the Producer's accuracy was only 5% which indicates that the classification result is very different from the initial geological map and there were other surfaces not reported and that may be assigned to the (Plm) unit.

To understand origin of inconsistency, spectral profiles of all lithostratigraphic units with statistics concerning minimum, maximum, mean and standard deviation of each MNF eigenimages were calculated. Resulting statistics indicates that lithostratigraphic limits drawn on geological maps were in reality mixed and indistinguishable. For example (M-Pl), (Qcl) and (a) units cannot be differentiated with all 14 MNF eigenimages (Fig. 9).

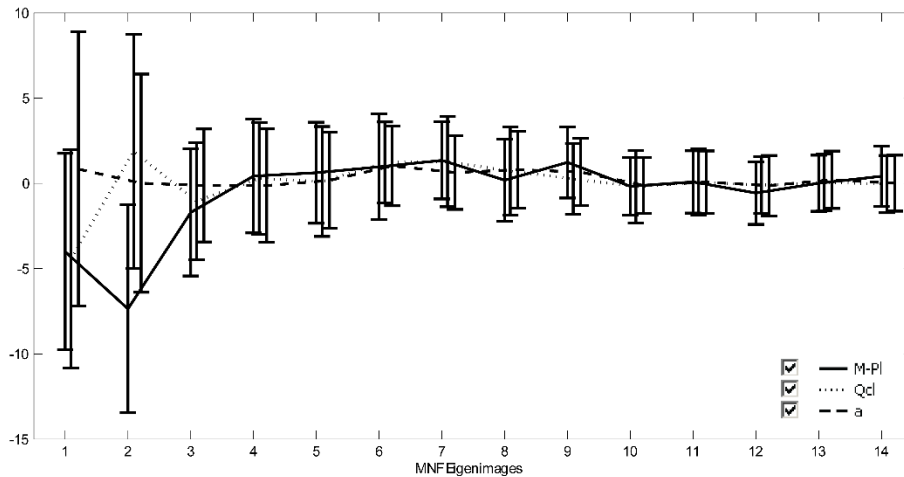


Fig. 9: 'M-Pl', 'Qcl' and 'a' spectral profiles

In addition, 391 reference sites were used to assess accuracy of classification result. Sites were picked randomly from visual image interpretation and verified on field.

Table 5: Classification accuracy assessment for SAM classification with 391 reference sites

| | M-Pl | Plm | QV | Qd | Qe | Qg | IQ | a | Total | User's accuracy (%) |
|--------------------------------|------|-------|------|-------|----|-----|-----|-------|-------|---------------------|
| M-Pl | 35 | 5 | 0 | 0 | 0 | 0 | 0 | 0 | 40 | 87.5 |
| Plm | 1 | 22 | 0 | 0 | 0 | 0 | 0 | 1 | 24 | 91.66 |
| QV | 1 | 0 | 36 | 0 | 8 | 0 | 0 | 1 | 46 | 78.26 |
| Qd | 0 | 0 | 0 | 29 | 12 | 0 | 0 | 0 | 41 | 70.73 |
| Qe | 0 | 0 | 0 | 0 | 9 | 0 | 0 | 0 | 9 | 100 |
| Qg | 0 | 0 | 3 | 0 | 1 | 49 | 0 | 1 | 54 | 90.74 |
| IQ | 0 | 0 | 0 | 12 | 0 | 0 | 78 | 0 | 90 | 86.66 |
| a | 1 | 3 | 0 | 0 | 6 | 0 | 0 | 77 | 87 | 88.5 |
| Total | 38 | 30 | 39 | 41 | 36 | 49 | 78 | 80 | 391 | |
| Producer's accuracy (%) | 92.1 | 73.33 | 92.3 | 70.73 | 25 | 100 | 100 | 96.25 | | |

The overall classification accuracy for lithostratigraphic units is 85.67% and the kappa coefficient is 0.791. Both the Producer's and the User's accuracy of (M-Pl), (Qg), (IQ) and (a) lithostratigraphic units are greater than 85% indicating good classification accuracy. All other units except (Qe) are associated with both Producer's and User's accuracy values over 70% indicating acceptable classification accuracy. Although User's accuracy of (Qe) was 100%, this unit is poorly identified and classified; the classification procedure does not allow its differentiation with the (Qcl) unit (Table 5).

V. Conclusion

Potentials of ASTER is evaluated using a combination of visible and near infrared (VNIR), short wave infrared (SWIR) ASTER and five computed indices for geological mapping in semi-arid region with low spectral surfaces. ASTER level 1B data were processed based on endmembers spectral signatures and band ratios in order to discriminate and classify them. The adopted methodology consists of two main steps: the first one (1) data pre-processing with cross-talk correction, calibration and radiance conversion, atmospheric and topographic correction, orthorectification and indices computing; the second step (2) classification process with minimum noise fraction transformation, pixel purity index, endmember extraction and SAM classification. Accuracy assessment is calculated with reference to 391 sites. The produced map is estimated to be accurate and allows validation and extension of geological map at 1/50.000 scale.

References

- [1]. A. Hirano, R. Welch and H. Lang, Mapping from ASTER stereo image data: DEM validation and accuracy assessment, *ISPRS Journal of Photogrammetry & Remote Sensing*, 57, 2003, 356–370.
- [2]. M. Abrams, S. Hook and B. Ramachandran, *ASTER User Handbook Version 2* (Jet Propulsion Laboratory/California Institute of Technology: California 2001).
- [3]. Y. Yamaguchi, A.B. Kahle, H. Tsu, T. Kawakami and M. Pniel, Overview of Advanced Spaceborne Thermal Emission and Reflection Radiometer (ASTER), *IEEE Transactions on Geoscience and Remote Sensing*, 36(4), 1998, 1062-1071.
- [4]. L.C. Rowan and J.C. Mars, Lithologic mapping in the Mountain Pass, California area using Advanced Spaceborne Thermal Emission and Reflection Radiometer (ASTER) data, *Remote Sensing of Environment*, 84(3), 2003, 350–366.
- [5]. R.D. Hewson, T.J. Cudahy, S. Mizuhiko, K. Ueda and A.J. Manger, Seamless geological map generation using ASTER in the Broken Hill-Curnamona province of Australia, *Remote Sensing of Environment*, 99(1-2), 2005, 159-172.
- [6]. R.D. Hewson, T.J. Cudahy and J.F. Huntington (2001) Geologic and alteration mapping at Mt Fitton, South Australia, using ASTER satellite-borne data, in: Geoscience and Remote Sensing Symposium, 2001. IGARSS '01. IEEE 2001 International, pp. 3.
- [7]. L.C. Rowan, J.C. Mars and C.J. Simpson, Lithologic mapping of the Mordor, NT, Australia ultramafic complex by using the Advanced Spaceborne Thermal Emission and Reflection Radiometer (ASTER), *Remote Sensing of Environment*, 99(1-2), 2005, 105-126.
- [8]. X. Zhang, M. Pazner and N. Duke, Lithologic and mineral information extraction for gold exploration using ASTER data in the south Chocolate Mountains (California), *ISPRS Journal of Photogrammetry & Remote Sensing*, 62, 2007, 271–282.
- [9]. C. Gomez, C. Delacourt, P. Allemand, P. Ledru and R. Wackerle, Using ASTER remote sensing data set for geological mapping, in Namibia, *Physics and Chemistry of the Earth*, 30, 2005, 97–108.
- [10]. Y. Ninomiya, B. Fu and T.J. Cudahy, Detecting lithology with Advanced Spaceborne Thermal Emission and Reflection Radiometer (ASTER) multispectral thermal infrared "radiance-at-sensor" data, *Remote Sensing of Environment*, 99(1-2), 2005, 127-139.
- [11]. S. Khomsi, M. Bédir, M. Soussib, M.G.B. Jemia and K.B. Ismail-Latrache, Mise en évidence en subsurface d'événements compressifs Éocène moyen-supérieur en Tunisie orientale (Sahel) : généralité de la phase atlasique en Afrique du Nord, *Comptes Rendus Géosciences*, 338(1-2), 2006, 41–49.
- [12]. H. Gabtni, Apport de la gravimétrie à l'étude des structures profondes du Sahel de Tunisie (cas de la région de Kairouan–Sousse–Monastir), *Comptes Rendus Géosciences*, 337, 2005, 1409–1414.
- [13]. F. Mejri, P.F. Burolet and A. Ben Ferjani, *Petroleum Geology of Tunisia a Renewed Synthesis* (ETAP: Tunis, Tunisia, 2006).
- [14]. M. Ben Haj Ali, Y. Jedoui, T. Dali, H. BenSalem and L. Memmi (1985) Carte géologique de la Tunisie à 1/500.000, in: S.G.d. Tunisie (Ed.), Office National des Mines, Tunis, Tunisia.
- [15]. P.F. Burolet, J.M. Mugniot and P. Sweeney, The Geology of the Pelagian Block: The Margins and Basins off Southern Tunisia and Tripolitania, in: A.M. Naim, W. Kanes, F. Stehli (Eds.), *The Ocean Basins and Margins*, Springer US, 1978) 331-359.
- [16]. S. Bouaziz, A. Sghari and M. Ben Akacha (2003) Carte géologique de la Tunisie à 1/50.000 : Feuille de Agareb (N°106), in: S.G.d. Tunisie (Ed.), Office National des Mines, Tunis, Tunisia.
- [17]. N. Bahrouni, Y. Houla and M. Fakhraoui (2007) Carte géologique de la Tunisie à 1/50.000 : Feuille de Mahares (N°115), in: S.G.d. Tunisie (Ed.), Office National des Mines, Tunis, Tunisia.
- [18]. Y. Houla, N. Bahrouni and M. Fakhraoui (2007) Carte géologique de la Tunisie à 1/50.000 : Feuille de Sidi Salah (N°98), in: S.G.d. Tunisie (Ed.), Office National des Mines, Tunis, Tunisia.
- [19]. A. Sghaier, *Analyse morphostructurale de la région de Mahdia-El Jem-Jébiniana (Tunisie orientale)*, Diplôme d'Etudes Approfondies. Département de Géologie, Faculté des Sciences de Tunis, Tunisia, 2004.
- [20]. G.R. Hunt and R.P. Ashley, Spectra of altered rocks in the visible and near infrared, *Economic Geology*, 74(7), 1979, 1613-1629.
- [21]. R.J.P. Lyon and E.A. Bums, Analysis of rocks and minerals by reflected infrared radiation, *Economic Geology*, 58(2), 1963, 274-284.
- [22]. R.K. Vincent, L.C. Rowan, R.E. Gillespie and C. Knapp, Thermal-infrared spectra and chemical analyses of twenty-six igneous rock samples, *Remote Sensing of Environment*, 4, 1975, 199-209.
- [23]. M. Abrams, The Advanced Spaceborne Thermal Emission and Reflection Radiometer (ASTER): data products for the high spatial resolution imager on NASA's Terra platform, *International Journal of Remote Sensing*, 21(5), 2000, 847-859.
- [24]. A. Mushkin and A. Gillespie (2004) Estimating subpixel surface roughness using remotely sensed stereoscopic data, in: Geoscience and Remote Sensing Symposium, 2004. IGARSS '04. Proceedings. 2004 IEEE International, pp. 1292-1295 vol.1292.
- [25]. Y. Ninomiya (2002) Mapping quartz, carbonate minerals, and mafic-ultramafic rocks using remotely sensed multispectral thermal infrared ASTER data, in: Thermosense XXIV, SPIE, Orlando, FL, USA, pp. 191-202.
- [26]. N. Goldshleger, E. Ben-Dor, Y. Benyamini, M. Agassi and D.G. Blumberg, Characterization of soil's structural crust by spectral reflectance in the SWIR region (1.2±2.5 μm), *Terra Nova*, 13, 2001, 12-17.
- [27]. P.N. Bierwirth and K.S. Pfitzner (2001) Identifying acid mine-drainage pollution at Captains Flat, NSW, using airborne HYMAP data, in: Geoscience and Remote Sensing Symposium, 2001. IGARSS '01. IEEE 2001 International, pp. 2563-2565 vol.2566.
- [28]. J.W. Rouse, R.H. Haas, J.A. Schell and D.W. Deering, Monitoring vegetation systems in the Great Plains with ERTS, Third Earth Resources Technology Satellite Symposium, Washington, D.C., 1973, 309-317.
- [29]. Y. Ninomiya (2004) Lithologic mapping with multispectral ASTER TIR and SWIR data, in: Sensors, Systems, and Next-Generation Satellites VII, SPIE, Barcelona, Spain, pp. 180-190.

- [30]. M.W. Matthew, S.M. Adler-Golden, A. Berk, G. Felde, G.P. Anderson, D. Gorodetzky, S. Paswaters and M. Shippert (2002) Atmospheric correction of spectral imagery: evaluation of the FLAASH algorithm with AVIRIS data, in: Applied Imagery Pattern Recognition Workshop, 2002. Proceedings. 31st, pp. 157- 163.
- [31]. Research Systems Inc(RSI), *ENVI Tutorials, ENVI Version 4.1*, (2004).
- [32]. B.E. Hubbard, J.K. Crowley and D.R. Zimelman, Comparative Alteration Mineral Mapping Using Visible to Shortwave Infrared (0.4–2.4 μm) Hyperion, ALI, and ASTER Imagery, *IEEE Transactions on Geoscience and Remote Sensing*, 41(6), 2003, 10.
- [33]. A.A. Green, M. Berman, P. Switzer and M.D. Craig, A Transformation for Ordering Multispectral Data in Terms of Image Quality with Implications for Noise Removal, *IEEE Transactions on Geoscience and Remote Sensing*, 26(1), 1988, 65-74.
- [34]. F. Qiu, M. Abdelsalam and P. Thakkar, Spectral analysis of ASTER data covering part of the Neoproterozoic Allaqi-Heiani suture, Southern Egypt, *Journal of African Earth Sciences*, 44, 2006, 169–180.
- [35]. J.A. Richards and X. Jia, *Remote sensing digital image analysis an introduction* (Springer: Berlin; Heidelberg; New York, 2006).
- [36]. R.G. Vaughan, S.J. Hook, W.M. Calvin and J.V. Taranik, Surface mineral mapping at Steamboat Springs, Nevada, USA, with multi-wavelength thermal infrared images, *Remote Sensing of Environment*, 99(1-2), 2005, 140-158.
- [37]. F.A. Kruse (1996) Geologic Mapping Using Combined Analysis of Airborne Visible/Infrared Imaging Spectrometer (AVIRIS) and SIR-C/X-SAR Data, in: in Proceedings, International Symposium on Optical Science, Engineering, and Instrumentation, SPIE Proceedings, pp. 24-35.
- [38]. D.A. Landgrebe, *Signal theory methods in multispectral remote sensing* (Wiley: Hoboken, N.J.; [Chichester], 2003).
- [39]. R.G. Congalton, A review of assessing the accuracy of classifications of remotely sensed data, *Remote Sensing of Environment*, 37(1), 1991, 35-46.
- [40]. R.W. Fitzgerald and B.G. Lees, Assessing the classification accuracy of multisource remote sensing data, *Remote Sensing of Environment*, 47(3), 1994, 362-368.
- [41]. L. Hubert-Moy, A. Cotonnec, L. Le Du, A. Chardin and P. Perez, A Comparison of Parametric Classification Procedures of Remotely Sensed Data Applied on Different Landscape Units, *Remote Sensing of Environment*, 75(2), 2001, 174-187.